PCCP

Accepted Manuscript

ROYAL SOCIETY OF CHEMISTRY

www.rsc.org/pccp

Journal Name

RSCPublishing

ARTICLE

Flux-assisted synthesis of $SnNb_2O_6$ for tuning photocatalytic properties

Cite this: DOI: 10.1039/x0xx00000x

Received 00th January 2012,
Accepted 00th January 2012

DOI: 10.1039/x0xx00000x

www.rsc.org/

Dalal Noureldine,[a] Dalaver H. Anjum,[b] and Kazuhiro Takanabe[a]*

A flux-assisted method was used to synthesize $SnNb_2O_6$ as a visible-light-responsive metal oxide photocatalyst. The role of flux was investigated in detail using different flux to reactant molar ratios (1:1, 3:1, 6:1, 10:1, 14:1) and different reaction temperatures (300, 500, 600 °C). The obtained products were characterized by X-ray diffraction (XRD), scanning electron microscopy (SEM), Diffuse Reflectance UV-Vis Spectroscopy, X-ray photoelectron spectroscopy (XPS), the Brunauer-Emmett-Teller method (BET), and High Resolution Scanning Transmission Electron microscopy (HRTEM). Flux-assisted synthesis led to tin niobate particles in the platelet morphology with smooth surfaces. The synthesized crystal showed 2D anisotropic growth along the (600) plane as the flux ratio increased. The particles synthesized with a high reactant to flux ratio (1:10 or higher) exhibited slightly improved photocatalytic activity for hydrogen evolution from an aqueous methanol solution under visible radiation ($\lambda > 420$ nm). The photo-deposition of platinum and PbO_2 was examined to gain a better understanding of electron and hole migration pathways in these layered materials. The HR-STEM observation revealed that no preferential deposition of these nanoparticles was observed depending on the surface facets of $SnNb_2O_6$.

Introduction

Energy demand has been increasing continuously in recent decades, and the world's energy consumption is expected to double by the year 2050.[1] This challenge has oriented scientific interest towards renewable energy sources that can both fulfill the global needs and address environmental problems and the risk of oil depletion.[2] Overall water splitting using photocatalysis has been introduced as a very promising candidate for future energy needs.[3-6] It produces a clean, renewable, and high-density energy carrier, i.e., hydrogen. Numerous metal oxide photocatalysts have been reported to split water with high efficiency under UV irradiation.[7-9] However, to efficiently utilize sunlight, absorption in the visible region should be utilized for photocatalysis.[10] One promising approach is to combine d^0 transition metals with metals that have s^2d^{10} electron configurations, such as Sn^{2+}.[11-14] The hybridization between O 2p and metal s^2 orbitals results in a more strongly negative potential of the valence band than in oxides with only an O 2p contribution, thus minimizing the band gap.

$SnNb_2O_6$ is a promising visible-light-responsive photocatalyst with a band gap of 2.3 eV.[15] It has been reported to evolve either hydrogen or oxygen using sacrificial agents,[16] suggesting that the band positions are suitable to achieve overall water splitting. The drawback of Sn^{2+} mixed metal oxide synthesis is that it suffers from the disproportionation of Sn^{2+} into Sn^{4+} and metallic Sn at high temperatures, which minimizes its activity when prepared by solid-state synthesis.[17] The required high temperature for the synthesis does not offer control over the surface properties of photocatalytic materials, such as size, morphology and roughness. It is well known that the surface is a crucial part of the photocatalyst, where both the oxidation of water and the reduction of protons take place. Therefore, new synthetic routes are required to allow better control of characteristics in final products.[18] For the synthesis of $SnNb_2O_6$ materials, hydrothermal methods[19,20] and microwave-assisted synthesis[21] have been used for dye degradation applications. The obtained products showed a visible response, but their synthesis method led only to low crystallinity.[19,21] Recently, $SnNb_2O_6$ synthesized by a hydrothermal method showed hydrogen evolution activity under visible light irradiation.[20] The sample obtained by this method showed low crystallinity, but subsequent treatment at 800 °C was found effective in increasing the crystallinity. Flux-assisted synthesis is practical because it enhances the level of control over the sizes, surfaces and morphologies of photocatalytic metal-oxide solids[18] achieved by dissolving the precursors in a eutectic salt that induces rapid diffusion and therefore the formation of products in shortened reaction times and at lower temperatures.[18] The usage of lower temperatures and shorter reaction times compared to solid-state synthesis saves energy

and reduces the cost, which is highly attractive in comparison with solid-state method.[15,16] More interestingly, the flux-assisted method leads to the unique preferential growth of a specific facet that generally has lower interfacial energy than the other facets, which results in special morphologies, such as sheets, plates and flower-like shapes, that may have a beneficial effect on the photocatalytic activity of the material.[22,23] Furthermore, this method leads to high crystallinity and non-defective materials via a recrystallization process that occurs while cooling down at certain temperatures. Controlling the rate of cooling greatly affects the final product.[24] While cooling, the product particles nucleate homogenously in the liquid phase, and the rate of cooling defines the number of nuclei and the size of the product crystals.[25] Kudo and coworkers reported the flux-assisted synthesis of $SnNb_2O_6$ starting from a $Sr_2Nb_2O_7$ perovskite structure with $SnCl_2$ as a molten salt.[26] The synthesis proceeds through an ion exchange mechanism where Sn^{2+} replaces the Sr^{2+}, resulting in a layered structure. However, they required a long reaction time (30 h), and the process of removing the excess $SnCl_2$ was quite difficult. They also reported the molten salt treatment of $NaNbO_3$ nanorods and Nb_2O_5 nanowires with $SnCl_2$, and the activity for hydrogen evolution using a sacrificial reagent was comparable to $SnNb_2O_6$ produced by solid-state synthesis.[27] There are many controllable factors, such as the choice of salt, the stoichiometric mixture, the heating temperature and the reaction time.[28] Therefore, it is important to investigate the effect of flux on the size, shape, crystallinity, and growth of $SnNb_2O_6$ to improve the photocatalytic activity.

In this work, we investigated the effects of flux ratio and synthesis temperature on the crystal growth of $SnNb_2O_6$ particles. The photocatalytic activity of the materials synthesized by the flux method was compared to the activity of the materials synthesized by the solid-state method. The unique plate-like morphology of the product was obtained by the flux-assisted method, and the separation of excited carriers through these plate-like structures was probed using nanoparticle photo-deposition by the reduction of Ag^+ and Pt^{4+} cations into Ag and Pt metal, respectively, as electron sites and the oxidation of Pb^{2+} into PbO_2 metal to track holes.

Experimental

Synthesis of $SnNb_2O_6$

Stoichiometric molar quantities of SnO (Sigma Aldrich, 99.99%) and Nb_2O_5 (Aldrich, 99.99%) were mixed homogenously by grinding for 20 min under an argon atmosphere. $SnCl_2$ (Aldrich, 99.99%) was added as a flux to provide different reactant to flux molar ratios (1:1-F, 1:3-F, 1:6-F, 1:10-F, 1:14-F, F stands for flux). The mixture was ground again for 10 min under an argon atmosphere. The obtained mixture was transferred to an alumina boat and heated inside a tubular furnace under nitrogen flow with a flow rate of 100 ml min^{-1}. Different reaction temperatures (300, 500, 600 °C) were tested for 10 h, followed by radiative cooling to room temperature. The obtained samples were then washed by stirring overnight in Milli-Q water (18.2 MΩ cm^{-1}) to remove the remaining flux $SnCl_2$. The obtained powders were dried at 70 °C. Solid-state synthesis was performed by grinding for 30 min and heating for 10 h at 800 °C, as reported previously.[15]

Characterization

Powder X-ray diffraction (XRD) patterns were recorded with a BRUKER D8 Advance diffractometer (DMAX 2500) using a Cu K_α energy source at 40 kV and 40 mA. Scanning Electron Microscopy characterizations were performed on a Nova Nano 630 scanning electron microscope (SEM) from FEI company. The electron beam energy was set to 5 keV before the start of analysis. SEM measurements were used to determine the morphology as well as particle size of the synthesized particles. The SEM specimens were prepared by suspending them in ethanol and dispersing them by sonication. A drop of the solution was then poured onto the SEM stub and was dried before observations. The N_2 sorption studies were conducted using a Micrometrics ASAP 2420 to determine the Brunauer-Emmett-Teller (BET) surface area. The ICP measurements were performed using an ICP-OES Varian 72 ES. Digestion of the material was performed in the microwave digestion milestone of model ETHOS1. Diffuse reflectance spectra were measured using a UV-Vis spectrometer with an integrating sphere (JASCO, U-best 570) and were demonstrated according to the Kubelka-Munk function. Raman spectra of $SnNb_2O_6$ were acquired using a NT-MDT NTEGRA nano- and micro-Raman spectrometer equipped with a He-Ne laser (λ=633 nm), two solid-state lasers (λ=532 nm and 473 nm) and a Peltier cooled CCD Andor iDus 420. All spectra were acquired using 532 nm as the exciting wavelength in the z(x,x)-z backscattering geometry. For X-ray photoelectron spectroscopy (XPS), an AMICUS/ESCA 3400 instrument from KRATOS analytical was used with dual Mg/Al anodes and an energy source at 12 kV and 10 mA, based on calibration against the carbon 1s photoelectron signal at 284.2 eV. Transmission electron microscopy (TEM) analysis of samples was also performed to investigate the crystal structure, particle size and elemental composition present in the samples. The TEM analysis was carried out by setting the microscope in scanning TEM (STEM) and was accomplished by employing an aberration corrected Scanning TEM (STEM) microscope of model Titan G^2 60-300-ST from FEI Company. The microscope was operated at 300 keV beam energy during the STEM investigations and was the co-efficient of spherical aberration of Condenser-2 lens was reduced to about 1 um to perform a high-resolution STEM analysis of the samples. The Fast-Fourier transform (FFT) analysis of the acquired micrographs were also calculated to measure the inter-planar d-spacings of the crystalline phases present in the samples. The entire STEM analysis was performed in Gatan Microscopy Suite (GMS v. 1.83) software package from Gatan, Inc. Elemental mapping was performed by using a post-column energy filter of model GIF Tridiem 863 from Gatan, Inc. The

microscope was set to EFTEM mode to reduce the image magnification so that the field-of-view on the GIF CCD is about the same as that of the image-plane of the pre-GIF CCD. The elemental maps are generated by using the Ag-N23, Nb-N23, Pt-O23, and Pb-O23 energy edges from the corresponding Ag, Nb, Pt, and Pb elements, respectively. Furthermore the so called jump-ratio method was employed to produce these maps.

Photocatalytic experiments

Hydrogen evolution experiments were performed using a recirculating reactor unit. The accumulated gaseous products were analyzed using a Shimadzu GC with a Molecular Sieve 5A column. Photocatalytic overall water splitting was performed under visible light irradiation using a 300 W Xe lamp (CM1) with cutoff filter L42 with wavelength range ($420 < \lambda < 1100$ nm, Fig. S8).The experiments were performed using 90 ml of H_2O, 10 ml of methanol and 100 mg of photocatalyst. Wet impregnation was used to load 1 wt% platinum from an aqueous solution of H_2PtCl_6. The sample was heated while stirring until the water completely evaporated. The obtained product was reduced under hydrogen flow at 250 °C for 1 h.

Photo-deposition of metals and/or oxides

Three types of depositions were conducted: single photo-reduction, single photo-oxidation, and simultaneous photo-oxidation and photo-reduction. All photo-depositions were performed similarly in the recirculating reactor unit in 100 ml of Milli-Q water and irradiated by a 300 W Xe lamp (CM1) with cutoff filter L42 ($420 < \lambda < 1100$ nm: photon distribution is shown in Fig. S8) under continuous stirring. After 10 h of photo-deposition, the obtained suspension was filtered and washed with Milli-Q water, then dried at 70 °C for 12 h. The resulting powders were examined by HR-STEM.

The photo-reduction of Ag nanoparticles was performed starting with 0.1 g of $SnNb_2O_6$ and 10 mM $AgNO_3$ solution with 0.2 g of La_2O_3 as a buffer to maintain an alkaline medium. The photo-oxidation of PbO_x was performed starting with aqueous $Pb(NO_3)_2$ solution as a precursor in the presence of $NaIO_3$ as an oxidizing agent. The simultaneous photo-deposition of both PbO_x and Pt was achieved using 5 wt% $Pb(NO_3)_2$ and H_2PtCl_4 combined, with respect to the $SnNb_2O_6$ material.[29]

Results and Discussion

Particle crystal structure

Fig. 1 shows the XRD patterns of the powders prepared by solid-state synthesis and by flux-assisted synthesis after being washed and dried. The powders prepared by solid-state synthesis at 800 °C showed the formation of $SnNb_2O_6$ with the Froodite structure (monoclinic) in a pure phase, and all peaks can be indexed from the PDF data (PDF-01-084-1810).[30] The synthesis at 800 °C was necessary to obtain the pure phase of $SnNb_2O_6$ because of the slow diffusion process during solid-state synthesis.[31] A trace amount of the precursor phases was observed in the XRD pattern for the sample synthesized by the solid-state method at 600 °C for 10 h (Fig. S1). The XRD pattern of the material synthesized by flux assisted synthesis at 1:1-F, showed a low crystalline nature of $SnNb_2O_6$ formation with a small amount of the starting material Nb_2O_5 remaining, indicating that this low flux ratio was not sufficient to form the $SnNb_2O_6$ crystal at 600 °C, which may be attributed to the low solubility of the precursors at this flux amount. At 1:3-F and 1:6-F small remaining starting material were observed as well, but they become negligible at high flux ratios. As the flux ratio increased, the peak intensity of the (600) plane exclusively increased, suggesting that the growth of the (600) plane was preferentially induced by the presence of flux along the (bc) plane.[27] This preferential growth can be explained by the presence of chloride ions in the molten salt, which may complex with Sn^{2+} ions and selectively lower the interfacial energy along this plane, making growth along this plane more favorable at the expense of other planes.[32,33]

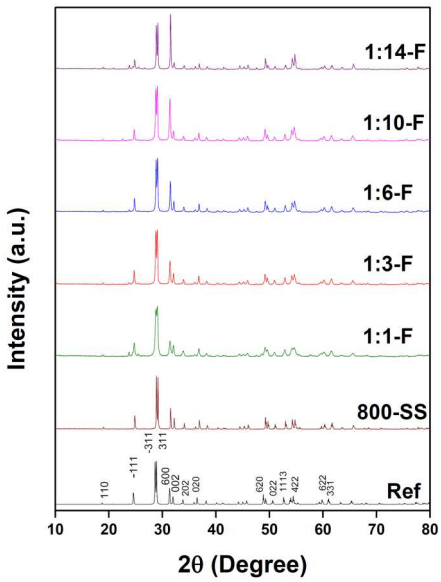

Fig. 1 XRD patterns of $SnNb_2O_6$ prepared by solid-state synthesis at 800 °C (800-SS) and by flux-assisted synthesis with different reactant ($SnO+Nb_2O_5$):flux ($SnCl_2$) molar ratios: 1:1-F, 1:3-F, 1:6-F, 1:10-F, and 1:14-F. Reference: ICSD (PDF-01-084-1810).[30]

The crystallinity of the main peaks increased with increasing flux ratio, and almost pure phase was obtained at the highest ratios (1:10) and (1:14) with only trace amount of remaining starting materials (2% estimated from the Reitveld analysis). This result confirms the beneficial effects of flux-assisted synthesis in that it leads to the desired products at lower temperatures than solid-state synthesis with the specific ability to induce preferential crystal growth by modifying the flux parameter. This ability is explained by the improved extent of dissolution of the precursors in the molten salt when the flux quantity was increased. To study the effect of temperature on the growth of the material, synthesis experiments were

conducted at lower temperatures (300 and 500 °C). At 500 °C, as the flux ratio increases from 1:1 to 1:14, the crystallinity of the main peaks also increases, and a single phase of $SnNb_2O_6$ was observed at high ratios (Fig. S2). The synthesis of single-phase $SnNb_2O_6$ was incomplete at 300 °C with ratios of 1:1-F, 1:3-F, and 1:6-F, and the XRD patterns show the main peaks of Nb_2O_5 and a mixture of SnO, SnO_2 and metallic Sn. Interestingly, even at a low temperature (300 °C), for the materials synthesized at a high flux ratio (1:10-F), the $SnNb_2O_6$ crystal phase was obtained with low crystallinity and remaining precursors (Fig. S3). Also the longer synthesis time (30 h) led to the enhanced crystallinity of $SnNb_2O_6$ (Fig. S3). This result suggests that $SnCl_2$ flux functions as the solution medium, lowering the chemical potential of the reactants to reach the liquid single-phase region. In this region of the phase diagram, it is anticipated that both reactants ($SnO+Nb_2O_5$) dissolve and their mobility increases.[25] The nucleation of $SnNb_2O_6$ product may begin in the liquid phase under high supersaturation, known as the solution-precipitation mechanism.[34] After nucleation, the obtained product continues to grow. The best known mechanism of growth is the Ostwald ripening,[35] the rate of which depends on the diffusion coefficient, the solubility, and the atomic structure.[35] A high diffusion coefficient and higher solubility of starting materials are generally attained at higher temperatures and higher ratios of the flux salt. In our study, the formation of $SnNb_2O_6$ was preferred at higher temperatures and higher flux ratios, consistent with this mechanism.

Morphological analysis

The morphology of semiconductor particles is affected by both the equilibrium and growth forms of the crystal.[36] The crystal structure generally determines the stable facets, and the particle shape is also influenced by the chemical composition of the crystal and the salt. The particles tend to grow towards equilibrium by minimizing the surface free energy, which is achieved mainly by dissolving the planes with high surface energy and growing the more stable planes. This process results in anisotropic growth along these low energy stable faces, which will have a lower growth rate and consequently afford well-developed facets.[32] To evaluate the effect of flux on the $SnNb_2O_6$ morphologies, SEM images of the products synthesized by both methods were compared. Fig. 2 shows the SEM images of $SnNb_2O_6$ synthesized by the molten salt flux-assisted method and by solid-state synthesis. The effect of the reactant to flux molar ratio can be clearly observed. At a low reactant to flux ratio (1:1), the obtained product began showing a plate morphology, but with limited anisotropic growth in the 2D dimension, which afforded aggregates with non-uniform particles ranging between 100 and 500 nm. This result can be explained by the lower solubility of the reactant particles at this low flux ratio. However, in the 1:3-F sample, the plate morphology was clearer and better defined, and the plate size was between 500 nm and 1 μm in length with a thickness of approximately 100 nm. At higher ratios (1:6-F, 1:10-F, 1:14-F), large plates with lengths 0.5-2 μm and thicknesses of approximately 100 nm were obtained. The increase in particle size is explained by the Ostwald ripening mechanism as prolonged heating at a higher flux ratio will increase the mobility and therefore the diffusion coefficient of the reactants. This results in a higher growth rate and larger particle size. [35] SEM of 800-SS confirms that the materials synthesized by the solid-state method showed irregular grain particles that form aggregates with increased grain boundaries. The sintering of the product particles synthesized by the solid-state method begins simultaneously with the formation of particles. This sintering can be avoided by the flux-assisted method, as the molten salt covers the surfaces of all particles and inhibits their agglomeration.[37] This advantage becomes more evident at high flux ratios, as it can be observed that the plates in the 1:6-F and 1:10-F samples have more uniform surfaces with fewer aggregates of small particles than 1:3-F and 1:1-F. The trend of particle growth and plate-like morphology was similarly observed in the lower-temperature synthesis (500 °C; Fig. S4). However, it can be clearly observed that the large plate-like particles have smaller plates on their surface at the ratios of 1:1-F, 1:3-F, 1:6-F. This result is explained by the lower growth rate at lower temperature[35] and indicates that the obtained morphology is a consequence of the molten salt flux.

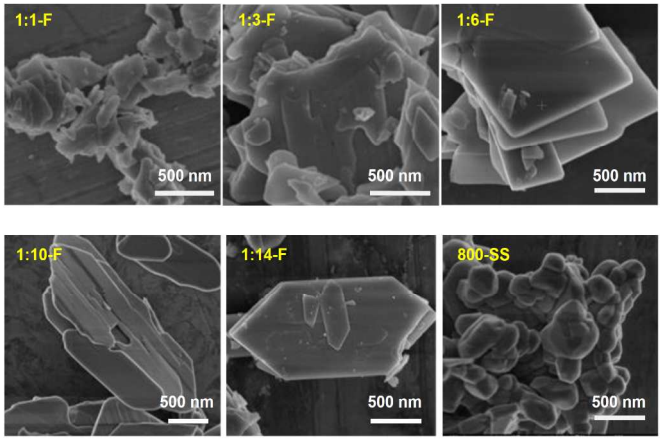

Fig. 2 SEM images of $SnNb_2O_6$ prepared by solid-state synthesis at 800 °C (800-SS) and by flux-assisted synthesis with different reactant ($SnO+Nb_2O_5$):flux ($SnCl_2$) molar ratios: 1:1-F, 1:3-F, 1:6-F, 1:10-F and 1:14-F.

Table 1 The synthesis temperature, Sn/Nb ratio from ICP, average particle size estimated from SEM images, and BET surface area for the samples synthesized at different flux ratios.

Reactant molar ratio, (SnO-Nb_2O_5) : $SnCl_5$	Temperature (°C)	Band gap (eV)	Sn/Nb (%)	Average particle size (μm)	Surface area (m^2 g^{-1})
1:1	600	2.1	0.49	0.3	6.1
1:3	600	2.46	0.49	0.5-1	4.1
1:6	600	2.44	0.49	1.5-2.0	6.6
1:10	600	2.45	0.49	1.5-2.0	5.2
1:14	600	2.45	0.55	2.0-3.0	4.4

800-SS	800	2.33	-	0.5	1.4

The particle size was estimated from the SEM images, and the results are summarized in Table 1. The BET surface areas of the synthesized materials are summarized in Table 1 as well. The material prepared by solid-state synthesis (800-SS) showed a surface area of 1.3 m^2 g^{-1}, similar to the reported value.[16] The samples synthesized by the flux-assisted method showed BET surface areas of 6.1, 4.1, 6.6, 5.2, and 4.4 m^2 g^{-1} for 1:1-F, 1:3-F, 1:6-F, 1:10-F, and 1-14-F, respectively.

Fig. 3 shows the diffuse reflectance UV-Vis spectra of $SnNb_2O_6$ synthesized at different flux ratios (1:1-F to 1:14-F) and in the solid state (800-SS). It can be seen that the samples prepared by the flux-assisted method show higher surface areas than the samples synthesized by the solid-state method, but the difference is not very large due to the similar particle sizes. $SnNb_2O_6$ powders prepared by the flux-assisted method have band gaps of 2.1, 2.46, 2.44, 2.45, and 2.45 for 1:1-F, 1:3-F, 1:6-F, 1:10-F, and 1:14-F, respectively, as summarized in Table 1. The sample prepared by solid-state synthesis (800-SS) has a band gap of approximately 2.33 eV, which also agrees with previous reports.[15]

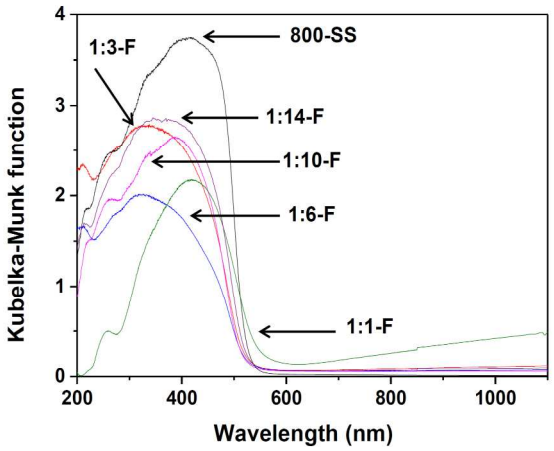

Fig. 3 DR.UV-Vis spectra of $SnNb_2O_6$ prepared by solid-state synthesis at 800 °C (800-SS) and by flux-assisted synthesis with different reactant ($SnO+Nb_2O_5$):flux ($SnCl_2$) molar ratios: 1:1-F, 1:3-F, 1:6-F, 1:10-F, and 1:14-F.

The distinctive absorption edges were observed in all cases, except for the sample with 1:1-F. For the 1:1-F sample, a slight red-shift in the absorption edge can be attributed to the presence of defects, as observed in XRD, where the unreacted precursors were still present (Fig. 1). As the flux ratio increased, the absorption edge was slightly blue-shifted. The absorption beyond the band gap of $SnNb_2O_6$ (baseline) decreased and was the lowest for the 1:10-F sample, which may imply a decrease in reduced species or defects. This minor band gap alteration (blue-shift) with intensive flux use may be correlated with improved plate-like morphology, where the crystal shows a 2D anisotropy while decreasing the thickness with respect to the length. This blue-shift was previously reported for the synthesis of Bi_2MoO_6 materials with a nanoplate-like morphology.[38] The Raman spectra of these samples (Fig. S5) were compared, and they all showed the same Raman shifts for Nb-O bonds, which further confirm that the blue-shift is due to the plate morphology rather than to structural differences. The band gaps of these materials were estimated from Tauc's plot (Fig. S6), and it was observed that the absorption edges of the samples from 1:3-F to 1:14-F are steep, indicating the transition from the valence to the conduction band.

Surface properties

Surface is an important parameter in designing any photocatalyst since all chemical reactions take place on it. To study the effect of flux on the surface, XPS measurements were conducted. Fig. 4 shows XPS spectra for the 1:10-F sample versus 800-SS. It was reported that binding energies of Sn $3d_{5/2}$ of Sn^{2+} (SnO) and Sn^{4+} (SnO_2) are 485.8 eV and 486.3 eV, respectively.[39] Clearer distinction between Sn^{2+} and Sn^{4+} is possible by Auger lines corresponding to $M_4N_{4,5}N_{4,5}$ transition, giving about 1.3 eV difference.[47-50]

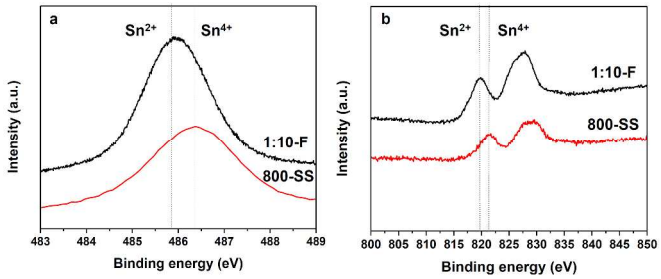

Fig. 4 XPS spectra for a) Sn $3d_{5/2}$ and b) Sn Auger peaks ($M_4N_{4,5}N_{4,5}$) of $SnNb_2O_6$ prepared by solid-state synthesis at 800 °C (800-SS) and by flux-assisted synthesis with a reactant ($SnO+Nb_2O_5$): flux ($SnCl_2$) molar ratio of 1:10-F.

It can be clearly observed in Figs. 4a and 4b that 1:10-F sample's surface is mainly composed of Sn^{2+} whereas 800-SS has larger amount of Sn^{4+}. This is explained by the difference in synthesis temperature. The higher temperature employed in solid state synthesis promoted the oxidation of the surface. However, the flux assisted synthesis enabled the formation of $SnNb_2O_6$ at lower temperature which prevented the oxidation of surface. This emphasizes the positive role of flux synthesis in minimizing surface states, and impurities. This effect is quite important since Sn^{4+} species acts as trap states for electrons which can decrease the activity of the material.[16]

Photocatalytic properties

Fig. 5 shows the photocatalytic activity for hydrogen evolution from 10% methanol aqueous solution using synthesized $SnNb_2O_6$ photocatalysts. It was observed that as the flux to reactant ratio increased, the photocatalytic activity for hydrogen evolution increased in parallel. The samples with 1:1-F and 1:3-F showed negligible activities (1 and 2.2 µmol h^{-1}, respectively). This result may be attributed to the presence of incomplete synthesis in the 1:1-F sample, which can be

observed in the DR.UV-Vis spectra (Fig. 3) and to the low crystallinity of these two samples, as shown by XRD (Fig. 1). It was observed that the sample 1:6-F gave high hydrogen amount (23 µmol) after 1 h but it decreased after the third hour to become lower than that of 800-SS. The samples prepared at the high flux ratio 1:10-F gave the hydrogen amount of about 34 µmol after 1 h, then reaching 158 µmol of hydrogen after 5 h. This is relatively higher than the 800-SS sample (15 µmol after 1 h, 122 µmol after 5 h). The hydrogen amount with the sample prepared with high flux ratio of 1:14-F was similar to that with the 1:10-F sample.

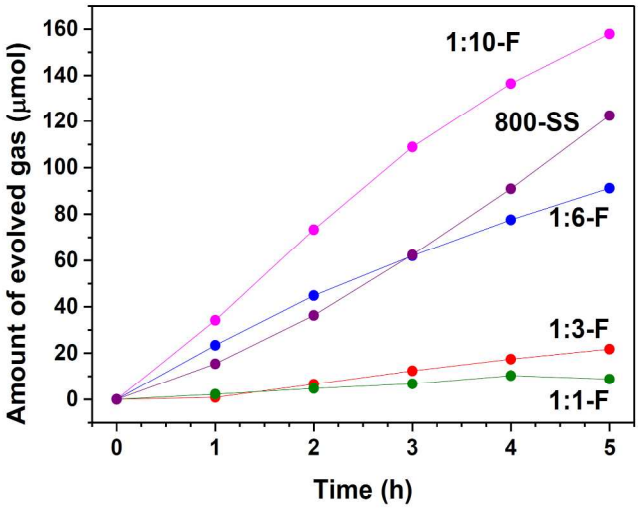

Fig. 5 Photocatalytic hydrogen evolution activities of $SnNb_2O_6$ prepared by solid-state synthesis at 800 °C (800-SS) and by flux-assisted synthesis with different reactant ($SnO+Nb_2O_5$): flux ($SnCl_2$) molar ratios: 1:1-F, 1:3-F, 1:6-F, and 1:10-F.

The improved hydrogen evolution activity can be explained by two factors. The first is the smoother surfaces with minimized grain boundaries obtained by the molten salt flux-assisted method in comparison with the agglomerated particles obtained by the solid-state method. Grain boundaries are generally considered to be electron recombination sites.[16] The second is the enhanced surface properties produced by the flux-assisted method, which afforded less oxidized surfaces. As discussed in the XPS section, the Sn^{4+} sites create local electronic states that are disconnected from the bulk (Sn^{2+}), thus functioning as trap sites for excited carriers.[16] The same trend for hydrogen evolution activity was observed at the lower temperature of 500 °C. This result emphasizes the role of the flux ratio as a control parameter for photocatalytic performance. To further confirm that the difference in photocatalytic activity does not originate from any difference in the composition of the samples, ICP quantitative analysis was performed. The results are summarized in Table 1. All the prepared samples have the same Sn/Nb ratio of 0.49, which nearly matches the theoretical ratio of 0.5. This result is consistent with the lack of extra Sn species from excess flux.

It is important to note that the Froodite $SnNb_2O_6$ crystal structure is known to be a layered material, as shown in Fig. 6. The crystal structure is made up of Nb_2O_6 edge-shared octahedra forming a two-octahedron-thick sheet with Sn^{2+} ions interlayered between the two sheets. Layered materials have been introduced by Domen and coworkers as a unique class of heterogeneous photocatalysts called "Two-Dimensional" photocatalysts.[40-42] They showed different behavior from conventional bulk semiconductor catalysts and were able to achieve overall water splitting with $K_4Nb_6O_{17}$ as the photocatalyst and nickel oxide as the cocatalyst. These materials have the advantage of having two types of periodic interlayers, called Interlayer I and Interlayer II. This structure allows water molecules to intercalate within the interlayers such that the reduction of water into hydrogen takes place on one side of the NbO_6 sheet (Interlayer I), while the oxidation of water takes place on the other side of the NbO_6 octahedra (Interlayer II). Adding ultrafine nickel particles as a hydrogen evolution cocatalyst within the interlayers enhanced the activity of the material by improving the extent of charge separation and minimizing electron-hole recombination.[43] Another family of layered materials called ion-exchangeable niobates with the general form of A ($M_{n-1}Nb_nO_{3n+1}$), where A= Na, K, Rb, Cs; M = La, Ca, was found to show improved photocatalytic activity.[43] This perovskite family has the ability to exchange alkaline metal ions with H^+ ions. This improved hydrogen evolution activity was attributed to the enhancement in the migration of reactant molecules within the interlayers.[43]

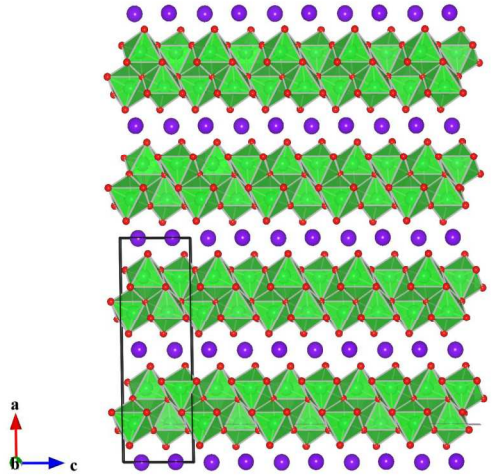

Fig. 6 Polyhedral model structures of $SnNb_2O_6$; Sn (purple sphere) and O (red sphere) with Nb-centered coordinate (green octahedra).

As concluded from XRD, the molten salt did lead to preferential growth along the (b,c) plane, which resulted in the plate-like morphology visible by SEM. Based on the similarity of structure between tin niobate materials and the reported layered materials, we investigated the effect of this anisotropic growth on the charge separation mechanism. To probe the electron-hole pair in this material, the photo-deposition of Ag, Pt, and PbO_x was examined by HR-STEM. It is known that under visible radiation, Pt^{4+} and Ag^+ will be photo-reduced into Pt and Ag metal nanoparticles, respectively, and they will act as electron acceptors, while Pb^{2+} will be oxidized into PbO_2 and

act as a hole acceptor.[29] Therefore, probing these metals/metal oxides on the surface of a semiconductor will provide insight into the active sites.[44] We performed three photo-depositions: 1) photo-reduction of Ag^{+} to track electrons, 2) photo-oxidation of Pb^{2+} to probe holes, and 3) simultaneous photo-oxidation of Pb^{2+} and photo-reduction of Pt^{4+}.

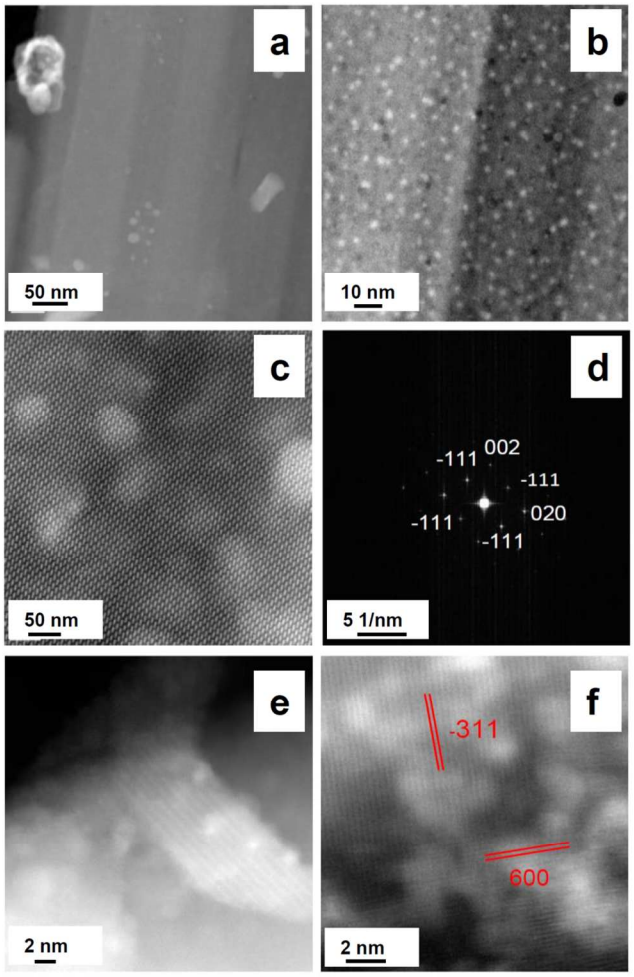

Fig. 7 (a) TEM image of $SnNb_2O_6$ (1:10-F) deposited with Ag particles, (b), (c) HRTEM images of $SnNb_2O_6$ (1:10-F) with Ag nanoparticles, (d) SAED of (c), (e) $SnNb_2O_6$ (1:10-F) deposited with PbO_x, and (f) $SnNb_2O_6$ (1:10-F) deposited with Pt and PbO_x simultaneously.

Fig. 7 shows HR-STEM micrographs, generated by using an high angle annular dark field (HAADF) detector that was attached above the projection chamber of the microscope, of $SnNb_2O_6$ with silver nanoparticles (a, b, c), PbO_2 (e) and both Pt and Pb (f). The surface of $SnNb_2O_6$ deposited with Ag shows a uniform morphology with minimum aggregates and a homogenous distribution of Ag (Fig. 7a). This uniform distribution of Ag nanoparticles is more obvious at higher magnification (Fig. 7b). This result suggests that the smooth morphology of the surface minimizes electron-hole recombination and enhances the activity of $SnNb_2O_6$ by providing homogenously distributed active sites with minimum grain boundaries. Fig. 7c shows HR-STEM micrographs of $SnNb_2O_6$ deposited with silver, where clear lattice fringes are observed. Fig. 7d shows the corresponding fast Fourier transform (FFT), which contain the frequencies of 0.35, 0.237 and 0.255 nm. These frequencies present correspond to (-111), (020) and (002) inter-planer d-spacings of the monoclinic $SnNb_2O_6$ structure, respectively.[45] It shows that the sample has single-crystalline character. Furthermore, the symmetry of the FFT shows that the crystal was oriented along the [110] zone-axis with respect to the direction of electron beam. Fig. 6e shows the sample on which the photo-oxidation of PbO_x occurred in the presence of iodate as the electron acceptor. It can be observed that PbO_x deposited randomly on the surface. It was further confirmed by Energy Dispersive Spectroscopy (EDS) that Pb species are present at various positions on the surface (Fig. S7), and there was no observed selective photo-deposition of PbO_x. When both Pt and Pb were present in the reaction medium, it was determined from the EDS spectra that Pt predominates on the surface (Fig. S7). It can be observed that Pt is deposited on both sets of planes (600) and (-311) with d-spacings of 0.29 and 0.34 nm, respectively.

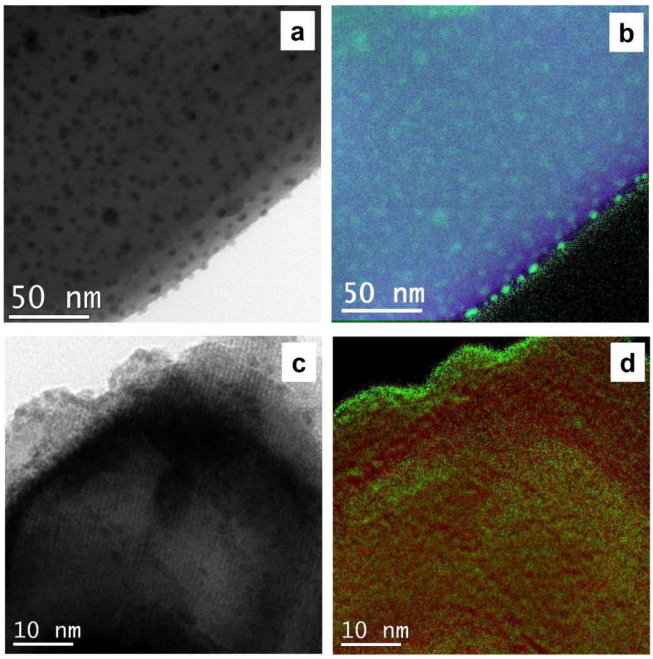

Fig. 8 (a) HR-TEM image of $SnNb_2O_6$ (1:10-F) deposited with Ag particles, (b) EFTEM mapping corresponding to a, (c) HR-STEM of $SnNb_2O_6$ (1:10-F) with Pt and PbO_x nanoparticles, (d) EFTEM mapping corresponding to c.

The HR-TEM and EFTEM mapping images of the Ag-deposited 1:10-F sample (Fig. 8a,b) confirms the uniform distribution of Ag nanoparticles on the flat surfaces and the edges (EFTEM: Ag in green). The mapping images of the $SnNb_2O_6$ (1:10-F) sample deposited with both Pt and PbO_x (Fig. 8c,d) gave highly dispersed Pt (green) neighboring PbO_x (red) deposited alternatively on the surface next to each other with no special separation or selective deposition. This

observation indicates that there was no selective charge separation on specific facets, and therefore, the morphology obtained by the flux-assisted method did not affect the charge separation mechanism in these layered materials. It also confirms that charge separation happens in a few nm scale, likely requiring further optimization of cocatalyst decoration on the surface (size, distance etc.) for improved photocatalysis.[51] For the 800-SS sample (Fig. S9a), the distribution of the deposited Ag particles was not as uniform and the large aggregates of Ag (~10 nm) were observed. Similar behavior was observed in the 800-SS sample deposited with PbO_x nanoparticles where they were deposited on the flat surface as well as on the edges (Fig. S9). This result confirms that the 800-SS sample possesses non uniform morphology which affects the non-uniform distribution of the potential active sites for hydrogen evolution and excited electron pathway. This result confirms that the role of flux is mainly in promoting the growth of the plate-like morphology with non-aggregated surfaces, and the preferential growth has no effect on the crystal structure and distribution of active sites for photocatalysis.

Conclusions

The role of flux-assisted synthesis using molten salt has been investigated as a means to control the surface properties. We successfully tuned the crystal morphology by increasing the flux to reactant molar ratio, which afforded defined particles with non-aggregated surfaces. The XRD patterns and SEM analyses confirmed a 2D anisotropic growth along the *bc* plane, providing a plate-like morphology as the flux ratio increased. The DR.UV-Vis spectra of the obtained samples were consistent with the formation of $SnNb_2O_6$ in a single phase. The photocatalytic activity for hydrogen evolution was enhanced as the flux ratio was increased, reaching the highest value at a 1:10-F ratio. This result was explained by the beneficial role of increased flux in allowing the formation of tin niobate at a lower reaction temperature than with solid-state synthesis. This heightened activity coincides with the minimized amount of Sn^{4+} on the surface boundaries, which may act as trap states. Furthermore, the flux-assisted method resulted in plate-like morphology with minimal aggregates. The molten salt flux-assisted synthesis provides a margin for control over surface properties, morphology, and defects that could increase the photocatalytic activity.

Notes and references

[a] *Division of Physical Sciences and Engineering, KAUST Catalysis Center (KCC), King Abdullah University of Science and Technology (KAUST), 4700 KAUST, Thuwal, 23955-6900 Saudi Arabia.*
[b] *Advanced Nanofabrication, Imaging and Characterization core lab, King Abdullah University of Science and Technology (KAUST), 4700 KAUST, Thuwal, 23955-6900 Saudi Arabia.*

Electronic Supplementary Information (ESI) available: More data for XRD patterns, SEM images, Raman spectra, Tauc's plot and HR-TEM images. See DOI: 10.1039/b000000x/

1 N. S. Lewis and D. G. Nocera, *Proc. Natl. Acad. Sci. USA*, 2007, **103**, 15729-15735.
2 O. Edenhofer, K. Seyboth, F. Creutzig and S. Schlömer, *Annu. Rev. Environ. Resour*., 2013, **38**, 169–200.
3 K. Takanabe and K. Domen, *Green*, 2011, **1**, 313–322.
4 K. Domen, J. Kondo, M. Hara and T. Takata, *Bull. Chem. Soc. Japan,* 2000, **73**, 1307.
5 K. Domen, *Korean J. Chem. Eng.,* 2001, **18**, 862.
6 H. Kato, *Catalysis today,* 2003, **78**, 561.
7 H. Kato, K. Asakura and A. Kudo, *J. Am. Chem. Soc.,* 2003, **125**, 3082.
8 A. Kudo, H. Kato and I. Tsuji, *Chem. Lett.* 2004, **33**, 1534.
9 J. Sato, H. Kobayashi, K. Ikarashi, N. Saito, H. Nishiyama and Y. Inoue, *J. Phys. Chem. B*, 2004, **108**, 4369.
10 K. Maeda, K. Teramura, D. Lu, T. Takata, N. Saito, Y. Inoue and K. Domen, *Nature*, 2006, **440**, 295.
11 D. Bodiot, *Rev. Chim. Miner.*, 1968, **5**, 569.
12 F. Brisse, D.J. Stewart, V. Seidl and O. Knop, *Can. J. Chem.*, 1972, **50**, 3648.
13 L.P. Cruz, J.M. Savariault, J. Rocha, J.C. Jumas and J. D. Pedrosa de Jesus *J. Solid State Chem.*, 2001, **156**, 349.
14 P. Cerny, A.-M. Fransolet, T. S. Ercit and R. Chapman, *Can. Mineral*, 1988, **26**, 889.
15 Y. Hosogi, K. Tanabe, H. Katol, H. Kobayashi and A. Kudo, *Chem. Lett*., 2004, **33**, 28.
16 Y. Hosogi, Y. Shimodaira, H. Kato, H. Kobayashi and A. Kudo, *Chem. Lett.*, 2008, **20**, 1299.
17 S. Uma, J. Singh and V. Thakral, *Inorg. Chem*., 2009, **48**, 11624.
18 K. Takanabe, K. Domen, *Chem. Cat. Chem.*, 2012, **4**, 1485 – 1497.
19 S. Liang, S. Zhu, Y. Chen, W. Wu, X. Wang, and L. Wu, *J. Mater. Chem.,* 2012, **22**, 2670.
20 S.W. Seo, T.H. Noh, S. Park, C.W. Lee, S. H. Kim, H. J. Kim, H.K. Park and K.S. Hong, *Int. J. Hydrogen Energy,* in press.
21 S. Liang, R. Liang, L. Wen, R. Yuan, L. Wu and X. Fu, *Appl. Catal. B,* 2012, **125**, 103-110.
22 E. K. Akdogan, R. E. Brennan, M. Allahverdi, A. Safari, *J. Electroceram.*, 2006, **16**, 159-165.
23 R. Amutha, M. Muruganandham, G. J. Lee, V. N. Batalova, G. Mokrousov and J.J. Wu, *Adv. Sci. Lett.*, 2010, **3** ,491-495.
24 C. F. Dickinson and G. R. Heal, *Thermochim. Acta*, 1999, **340 – 341**, 89 – 103.
25 T. Kimura, Molten Salt Synthesis of Ceramic Powders, In Advances in Ceramics - Synthesis and characterization; C. Sikalidis, Ed. InTech, Rijeka, Croatia, 2011.
26 Y. Hosogi, H. Kato and A. Kudo, *Chem. Lett.*, 2006, **35**, 578.
27 K. Saito and A. Kudo, *Inorg.Chem,* 2013, **52**, 5621.
28 D.H. Arney, Flux Synthesis of photocatalytic Transition Metal Oxides. Ph.D. Thesis, North California State University, Raleigh, NC, 2011.
29 R. Li, F. Zhang, D. Wang, J. Yang, M. Li, J. Zhu, X. Zhou, H. Han and C. Li, *Nat. Commun.* 2013, **4**, 1-7.
30 O. I. Velikokhatnyi and P. N. Kumta, *Can. Mineral.*, 1988, **26**, 899.
31 H. Schmalzried, In Chemical Kinetics of Solids, VCH, Weinheim, 1995.
32 B. Liu, J. Ma, H. Zhao, Y. Chen and H. Yang, *Appl. Phys. A.*, 2012, **107**, 437-443.

33 T. Kimura and T. Yamaguchi, *J. Mater. Sci.*, 1982, **17**, 1863-1870.
34 Y. Hayashi, T. Kimura and T. Yamaguchi, *J. Mater. Sci.*, 1986, **21**, 2876-2880.
35 M. N. Rahaman, Ceramic Processing and Sintering (2nd edition), Marcel Dekker, ISBN 0-8247-0988-8, New York, USA, 2013.
36 D. Elwell and H. J. Scheel, Academic Press, ISBN 0-12-237550-8, London, UK.
37 D.E. Niesz and R.B. Bennett, Structure and Properties of Agglomerates, In: Ceramic Processing Before Firing, G. Y. Onoda, Jr. & L. L. Hench, (Ed.), pp. 61-73, John Wiley & Sons, ISBN 0-471-65410-8, New York, USA.
38 J. Yu and A. Kudo, *Chem. lett.*, 2005, **34**, 1528.
39 G. Pang, H. Jin, Y. Li, Q. Wan, Y. Sun, S. Feng, *J. Mater. Sci.* 2006, **41**, 1429.
40 K. Domen, A. Kudo, A. Shinozaki, A. Tanaka, K-I. Maruya and T. Onishi, *J. Chem. Soc., Chem., Commun.,* 1986, 356.
41 A. Kudo, K. Sayama, A. Tanaka, K. Asakura, K. Domen, K. Maruya and T. Onishi, *J. Catalysis*, 1989, **120**, 337-352.
42 K. Domen, A. Kudo, A. Tanaka and T. Onishi, *Catal. Today*, 1990, **8**, 77-84.
43 K. Domen, J. Yoshimura, T. Sekine, A. Tanaka and T. Onishi, *Catal. Lett*., 1990, **4**, 339-344.
44 E. Bae and T. Ohno, *Appl. Catal. B. Environ.*, 2009, **91**, 634-639
45 T.S. Ercit and P. Cerny, *Can. Mineral*., 1988, **26**, 899.
46 K. Momma and F. Izumi, "VESTA 3 for three-dimensional visualization of crystal, volumetric and morphology data, *J. Appl. Crystallogr.*, 2011, **44**, 1272-1276.
47 J.-M. Themlin, M. Chtaïb, L. Henrard, P. Lambin, J. Darville and J.-M. Gilles, *Phys. Rev. B: Condens. Matter Mater. Phys.*, 1992, **46**, 2460-2466.
48 J.-M. Thermlin, J.-M. Gilles and R.L. Johnson, *J PHYS IV*, 1994, **4**, 183-186.
49 M. Stranick and A. Moskwa, *Surface Science Spectra*, 1993, **2**, 50-54.
50 M. Stranick and A. Moskwa, *Surface Science Spectra*, 1993, **2**, 45-49.
51 Y. Nakato, K. Ueda, H. Yano, H. Tsubomura, *J. Phys. Chem.*, 1988, **92**, 2316-2324.

Graphical abstract

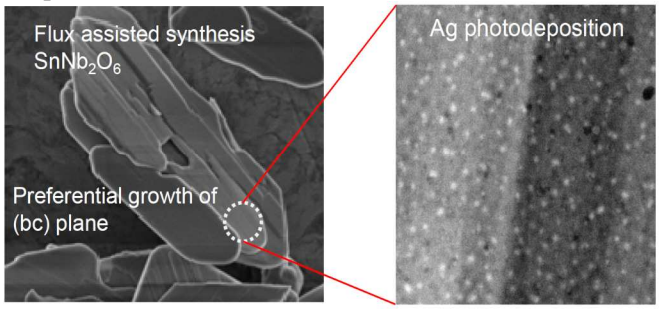

Flux assisted synthesis of $SnNb_2O_6$ facilitates growth of (bc) plane, which alters photocatalytic properties.